



Revealing electron numbers-binding energy relationships in heterojunctions via in-situ irradiated XPS

Yukun Li^a, Yongshang Zhang^b, Ruohan Hou^a, Yinyin Ai^a, Meng Cai^a, Zuhao Shi^c, Peng Zhang^{a,*}, Guosheng Shao^a

^a State Center for International Cooperation on Designer Low-carbon & Environmental Materials (CDLCEM), School of Materials Science and Technology, Zhengzhou University, Zhengzhou, Henan Province, PR China

^b School of Material and Chemical Engineering, Zhengzhou University of Light Industry, Zhengzhou, Henan 450001, PR China

^c State Key Laboratory of Silicate Materials for Architecture, Wuhan University of Technology, Wuhan 430070, PR China

ARTICLE INFO

Keywords:

Heterojunction
Electron transfer
In-situ irradiated XPS
Photogenerated electrons

ABSTRACT

Photogenerated charge transfer from photocatalysts to surface sites is a crucial step in guaranteeing photocatalytic efficiency, however, comprehending this process remains a challenge. While in-situ irradiated XPS (ISI-XPS) can function as a powerful method to investigate the electron transfer route and briefly determine the electron quantity under simulated photocatalytic conditions, the precise amount of transferred photogenerated electrons is still unknown. Based on an oxygen-doped ZnIn₂S₄ nanosheet on carbon nanofibers heterostructure catalysis, we discovered a potential means of calculating the precise quantity of photogenerated electrons through ISI-XPS. Additionally, we further propose a parameter to describe how many photogenerated electrons can participate in the photocatalytic reaction in conjunction with performance under monochromatic light and the corresponding electron count. Concurrently, the oxygen dopants serve as active sites to enhance the photocatalytic reaction process. This study presents a fresh outlook on the utilization of ISI-XPS and imparts a more profound understanding of the mechanism.

1. Introduction

The identification of the charge transfer process at the heterogeneous interface is essential in enhancing the stability, activity, and selectivity of heterojunction catalysts, thereby optimising the catalytic activity and efficiency [1–4]. In the case of photocatalysts, the transportation pathway and reaction sites of photogenerated electrons at heterogeneous interfaces are pivotal in driving photocatalytic reactions [5–10]. In recent years, the in-situ irradiated X-ray photoelectron spectroscopy (ISI-XPS) has emerged as an influential technique to monitor the activities of photogenerated electrons [11–16]. To demonstrate that the ISI-XPS had the capacity of direct observation of the migration path of photogenerated electrons, we constructed a TiO₂/Ti₃C₂ heterostructure in our previous work [17]. In addition, the ISI-XPS technique has been widely expanded to cover intricate ternary heterojunction systems, single-atom systems, and dual-single atom systems [18–22]. This approach offers a significant advantage in studying the conversion of electron density in photocatalytic processes due to its high sensitivity to changes in the chemical environment. However, the primary

applications of ISI-XPS concentrate solely on the electron transfer pathway according to published works, lacking any further exploration. Therefore, a thorough comprehension of ISI-XPS is crucial to its more effective utilisation for photocatalyst design.

Whilst there is no definitive relationship between the shift of binding energy and the amount of photogenerated electron transfer, our recent work has demonstrated that changes in valence state and binding energy follow an asymptotic function model [23–25]. However, the specific amount of electron transfer is not yet mentioned [26]. The motion of photogenerated electrons alters the outer electrons density, thus modifying the valence state of specific elements. A significant approach for investigating the light-responsive nature of photocatalysts is to combine binding energy with electron transfer numbers. To obtain accurate amounts of photogenerated electrons from various wavelength irradiations, valence states are utilized. Using the principles of XPS testing, we derive the precise number of electrons from the valence states. Accurately quantifying the transfer of photogenerated electrons is crucial to the evaluation of catalysts.

On the other hand, the number of photogenerated electrons that can

* Corresponding author.

E-mail address: zhangp@zzu.edu.cn (P. Zhang).

<https://doi.org/10.1016/j.apcatb.2024.124223>

Received 14 March 2024; Received in revised form 13 May 2024; Accepted 21 May 2024

Available online 22 May 2024

0926-3373/© 2024 Elsevier B.V. All rights are reserved, including those for text and data mining, AI training, and similar technologies.

partake in the reaction is uncertain. To achieve excellent photocatalytic performance in light-driven water splitting, the co-catalyst plays a critical role. It not only facilitates spatial separation of photogenerated electron-hole pairs but also offers additional active sites for the photocatalytic reaction. However, the sluggish reaction kinetics and slow desorption rate lead to the relaxation of those photogenerated electrons with photocatalytic ability, resulting in their return to the ground state [27,28]. Consequently, this issue causes a significant decrease in the utilization rate of photogenerated electrons during the photocatalytic process [29,30]. The phenomenon inspires the need for a deeper comprehension of photocatalytic reaction mechanism and a detailed co-catalyst function study during the reaction, which is important to optimising heterostructure photocatalyst. Unfortunately, not many studies have investigated this matter to date. Shedding light on the use of photogenerated electrons can enhance future photocatalyst design.

In this study, oxygen-doped ZnIn_2S_4 (ZIS) is loaded onto carbon nanofibers (CNFs) as a model photocatalyst. The aim is to offer a systematic investigation into the dopant's role and provide new insights into the behavior of photogenerated electrons under light excitation. To the best of our knowledge, this is the first time such an investigation has been conducted [31–36]. To achieve this, the study uses an ISI-XPS apparatus that comes equipped with a continuously adjustable wavelength irradiation light source. The apparatus's primary objective is to observe photogenerated electron actions on CNFs and O doping sites under specific wavelengths of light ranging from visible to ultraviolet. By means of this method, it is evident that the change in binding energy of the annealed sample is perpetually greater than that of the pristine sample under identical conditions, indicating an increase in electron density from the dopant. Furthermore, we suggest a parameter that, when combined with the apparent quantum yield, can portray the number of photogenerated electrons involved in the photocatalytic reaction. Based on this parameter, we conclude that the O dopants act as active sites that facilitate the reduction process. Our research presents a comprehensive analysis of ISI-XPS in doping studies and highlights the behavior of photogenerated electrons when subjected to light irradiation.

2. Experimental section

2.1. Materials and chemicals

polyacrylonitrile (PAN) with average Mw 150000, $\text{Zn}(\text{CH}_3\text{COO})_2$ were purchased from Macklin. N,N-Dimethylformamide (DMF), $\text{In}(\text{NO}_3)_3 \cdot 4.5\text{H}_2\text{O}$, thioacetamide, ethanol, glycerol were purchased from Sinopharm. Nafion solution (5 wt%) was purchased from Sigma-Aldrich.

2.2. Synthesis of catalysts

The preparation of carbon nanofibers (CNFs): Firstly, 0.6 g polyacrylonitrile (PAN) was dispersed into N, N-Dimethylformamide DMF (8 mL) solution and stirred till the PAN was completely resolved. Then the obtained precursors solution was drawn into the injector. The distance between the needle tip and collector plane was about 15 cm. The positive and negative voltage was set at 12 kV and −3 kV, respectively. At last, the as-prepared precursor was calcined first at 250 °C in muffle for 60 min with a rate of 2 °C·min^{−1} to pre-oxidize. After the pre-oxidation sample is cooled to room temperature, it is placed in a tubular furnace for carbonization. The carbonization condition is 800 °C for 2 h, and the heating time is 160 min.

The preparation of O doping ZIS/CNFs composite: The composite was synthesis via a facial hydrothermal and annealing approach. Weight 336 mg $\text{In}(\text{NO}_3)_3 \cdot 4.5\text{H}_2\text{O}$, 130 mg $\text{Zn}(\text{CH}_3\text{COO})_2$ and 180 mg thioacetamide and add them to 15 mL of ethanol containing 5 g of glycerol. After the above reagents are dissolved, add 80 mg of carbon fiber and stir for another 30 min. After completion, it is introduced into 100 mL Teflon-lined stainless steel autoclave, and react at 200 °C for 4 h. The

pristine sample is obtained after centrifugal and washing. Weigh 50 mg of the prepared composite photocatalytic material and place it in an alumina crucible. Heat it in a muffle furnace at a rate of 5 °C/min to the specified temperature and keep it for 1 h [37–39]. After the insulation is completed, cool it naturally to room temperature and take it out. Name the composite photocatalyst samples heated to 100 °C, 200 °C, and 300 °C as ZC-1, ZC-2, and ZC-3, respectively. The sample ZIS-100, ZIS-200 and ZIS-300 was obtained without CNFs under the same temperature treatment.

2.3. Sample characterization

XRD (Rigaku Ultima IV) data were applied to study the crystallinity under a scanning rate of 4°·min^{−1} from 10° to 80° by Cu-K α radiation ($\lambda=0.154178$ nm) and 45 kV and 40 mA. X-Ray photoelectron spectroscopy (XPS, AXIS UltraDLD, Kratos Analytical Inc) was used to investigate the chemical state photo-generated electrons migration pathway across the interface of heterostructure photocatalyst. The field emission scanning electron microscopy (SEM, FESEM, JSM-7500 F) was used to investigate the morphologies of the prepared samples. And the morphologies and structure were also studied through transmission electron microscope (TEM, FEI Tecnai G2 F20). The continuous tunable wavelength light source was PLS-EM 150 (Beijing Perfectlight Co. Ltd.). UV-Vis spectrophotometer (Shimadzu, model UV 3600) was taken to characterization all samples.

2.4. Photocatalytic activity performance

Photocatalytic solar fuel produce rate was measured by gas chromatography (GC-2014, Shimadzu). The photocatalytic hydrogen evolution reaction was carried out in a quartz reactor. And 300 W Xe lamp (MC-PF800B, Beijing MerryChange Technology CO. LTD.) was selected as a visible light and solar light source. Generally, the 20 mg sample, 50 mL deionized water and 10 mL triethanolamine (anhydrous, Sinopharm Chemical Regent, 99.5 %) was added into the quartz reactor with a stirring. The 300 W Xe lamp was used to illuminate the quartz reactor after purging with Ar. The gas chromatography was equipped with a thermal conductivity detector (TCD) and flame ionization detector (FID) to detect H_2 and CO and CH_4 which generated from quartz reactor via liquid suspension reaction, respectively.

The apparent quantum efficiency was calculated using equation

$$\text{AQY} = \frac{\text{Number of reacted electrons}}{\text{Number of incident photons}} \times 100\%$$

$$= \frac{2 \times n_{\text{H}_2}}{\frac{P \times t \times \lambda}{h \times c}} \times 100\%$$

where n_{H_2} represent the number of evolved H_2 molecules; P denotes the light power; $t = 9000$ s is the illumination time; the wavelength of incident light is denoted as λ ; h (6.63×10^{-34} J·s) denotes the Planck constant; and c (3.0×10^8 m·s^{−1}) means light speed.

2.5. Electrochemical measurement

Electrochemical performance was characterized through an electrochemical workstation (CHI-760E, CH Instruments Shanghai China) in a cubic quartz reactor. The 1 M Na_2SO_4 aqueous solution as electrolyte. The Pt tablet served as a counter electrode and the Ag/AgCl electrode acted a reference electrode. The F-doped tin oxide (FTO) glass coated with photocatalyst sample was the working electrode. The mixture including deionized water (225 μL), methanol (75 μL) nafion solution (30 μL). Then take 100 μL of the prepared solution and drop it on the area of 1×1 cm² of FTO glass. After it is naturally dried to form a dense film, conducting electrochemical test. A 300 W Xe lamp (MC-PF800B, Beijing MerryChange Technology CO. LTD.) was served as the light

source.

2.6. ISI-XPS measurement

The ISI-XPS was carried out on AXIS SUPRA UltraDLD. The continuous tunable wavelength light source was PLS-EM 150 (Beijing Perfectlight Co. Ltd.). In a typical test, the dark environment binding energy was characterized with all lights turned off in the SAC chamber. Then turn on the irradiation light source, set the wavelength to 700 nm, and conduct the test. After one round of test, reduce the wavelength by 50 nm and continue the test. Finish the test until the test wavelength was reduced to 350 nm.

2.7. XPS imaging

The XPS imaging was carried out on AXIS SUPRA UltraDLD. In excitation settings, the tuning set as imaging and the emission current was 15 mA. In tuning settings, the collimation mode was set as high res imaging, lens mode was set as FOV2 imaging and the resolution was set as 160. The binding energy of Zn 2p was set as 1018.32 eV and In 3d was set as 441.71 eV.

2.8. DFT calculation details

All calculations were performed using the first principles as implemented in the VASP code. The exchange-correlation functional was utilized at the generalized gradient approximation (GGA-PBE) level, projector augmented wave (PAW) methods were employed for the pseudopotentials. The reciprocal space was sampled with a $3 \times 3 \times 1$ Gamma mesh, and the DFT-D3 method was employed to consider the van der Waals interaction. The vacuum space in the z-direction was set to at least 15 Å in order to prevent the interaction between periodic images. The atomic structures and electronic properties were analyzed using the VESTA code.

3. Results and discussion

3.1. Mechanism of ISI-XPS and photocatalyst design

For photocatalytic materials, the most crucial step was the separation of photogenerated electron-hole pairs [40–44]. Numerous attempts were made to achieve this aim, among which the composite of co-catalysts was the most frequent and expedient method. However, due to the unfavorable carrier dynamics and thermodynamic performance, the photogenerated electrons migrating to the surface of the cocatalysts

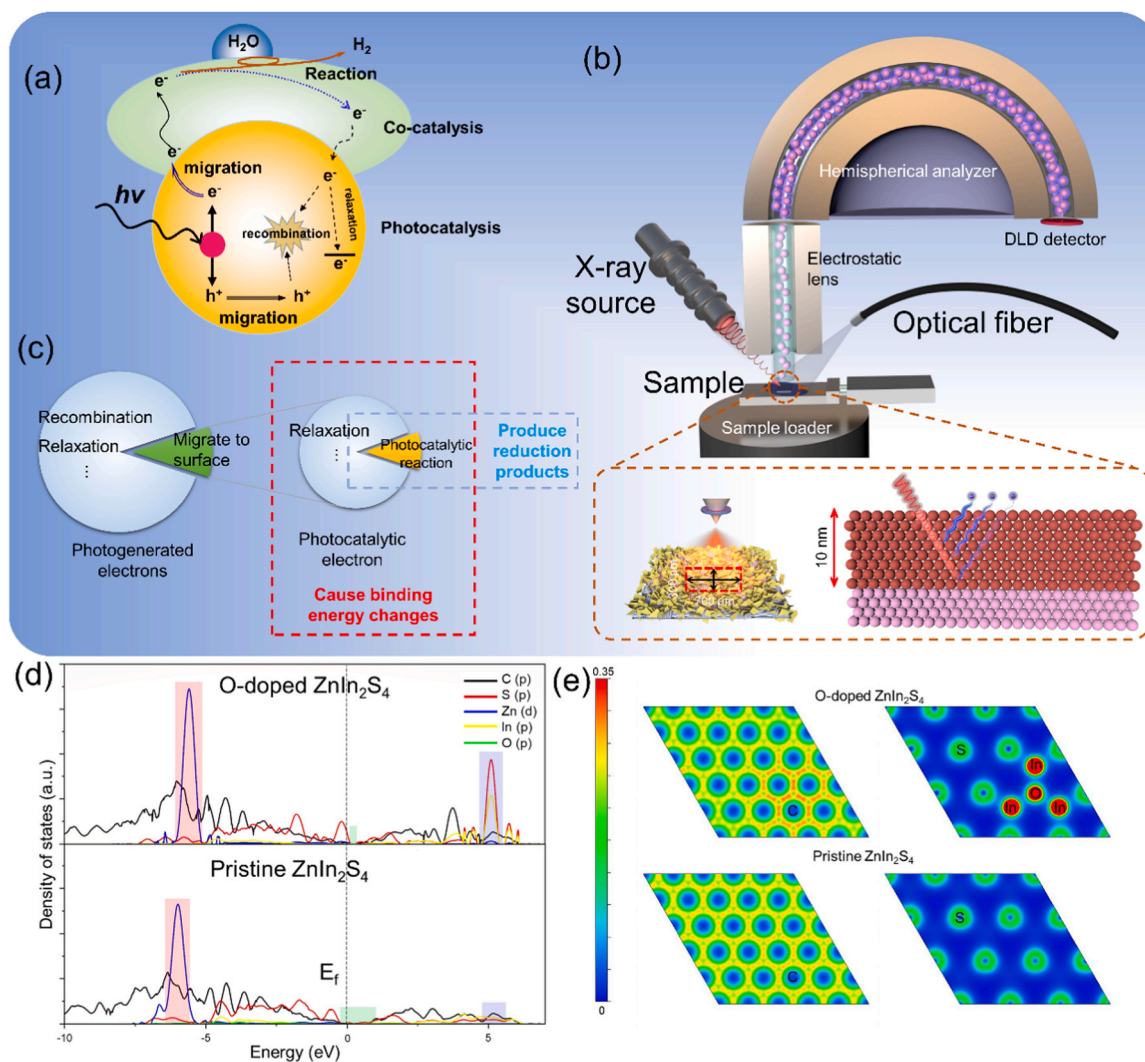


Fig. 1. (a) Photogenerated electrons behavior in photocatalysts. (b) Illustration of ISI-XPS measurement. (c) The relationship between Binding energy and photogenerated electrons. (d) Calculated density of states (DOS) of the O-doped ZIS slab and pristine ZIS slab. E_f —Fermi level. (e) The corresponding charge density distributions around the VBM of the O-doped ZIS slab and pristine ZIS slab, plotted from 0 (blue) to 0.1 Å (red).

failed to react in time and then suffered recombination or returned to the ground state (Fig. 1a). The efficacy of ISI-XPS, as an insightful approach for assessing photogenerated charges, had been established through numerous studies. To perform in-situ analysis, an external light source was introduced on an ex-situ basis. A typical test utilized an analytical area of $300 \times 700 \mu\text{m}$ and reached a depth of 10 nm (Fig. 1b). The migration of photogenerated electrons disrupted the electron density of the outer layer, contributing to changes in binding energy values. But not all photogenerated electrons that caused changes in binding energy participate in the reduction reaction, which made it difficult to gauge their actual reaction capability. This, in turn, lead to apparent binding energy changes (Fig. 1c). This resulted in the fact that the binding energy changes during actual testing could not truly reflect the catalytic ability of the material. Hence, clarifying the actual number of electrons involved in the reaction was pivotal in future research and design of photocatalysts.

Based on the preceding discussions, we first used a model of ZIS ultrathin nanosheet and its oxygen-doped counterpart with only a few layer as templates to demonstrate the aforementioned considerations. DFT calculations elucidated the impact of O doping on the electronic structure of the ZIS nanosheet. In the simulation model, we replaced a S atom near In atoms with an O atom to replicate the introduction of O atom (Fig. S1). According to the density of states results, as shown in Fig. 1d, the band gap of O-doped ZIS was absolutely narrowed compared to pristine ZIS, indicating an enhanced ability of light absorption to produce more photogenerated carriers. Due to the introduction of oxygen atoms, the O-doped ZIS exhibited a significantly higher charge density around the valence band maximum (VBM) and conduct band minimum (CBM) in comparison to the pristine ZIS. As a result, the O-doped ZIS nanosheets were capable of producing a greater number of charge carriers, which could directly participate in the catalytic reaction, resulting in significant improvement in their photocatalytic capabilities. The aforementioned discussion was further validated by the computed partial charge density prior to and post-doping (Fig. 1e). In this instance, the charge density was primarily derived from sulfur atoms for both pristine and O-doped ZIS. In this scenario, the charge density was predominantly derived from both sulfur and indium atoms for O-doped ZIS and pristine ZIS. Due to the incorporation of oxygen atoms, the O-doped ZIS displayed a significantly increased charge density around the valence band maximum compared to the pristine ZIS. This implied that the O-doped ZIS could generate many more charge carriers that may take part in the photocatalytic reaction, ultimately leading to a significant improvement in photocatalytic performance.

3.2. Synthesis and characterization of O-doped ZnIn_2S_4 /CNFs

The composite was formulated using a two-step approach (Fig. S2). The CNFs were prepared by means of electrospinning and calcination. The composite photocatalyst was synthesized through hydrothermal methods with oxygen doping achieved by retaining the temperature in a muffle furnace at varied temperatures. The XRD pattern showed the phase structure of the samples that were prepared (Fig. S3). All diffraction peaks were successfully indexed to the hexagonal phase of ZnIn_2S_4 (JCPDS 04-009-4787). The crystal planes (006), (102), and (110) displayed three major diffraction peaks at $2\theta = 27.69^\circ$, 21.59° , and 47.17° , correspondingly, in pristine ZC. The diffraction pattern of ZC stayed largely unaltered during annealing, suggesting the crystal structure remained unaffected. Fig. S4 outlined the Raman spectrum of pure ZIS and ZC composites. Due to the significant vibration intensity of CNFs, other vibration peaks were hardly observable (Fig. S4a). Consequently, pure ZIS, without CNFs, was utilized to examine its inherent vibration. The results revealed the existence of two principal peaks at 240 and 345 cm^{-1} , linked to ZIS. The small variation observed at 340 cm^{-1} in the Raman spectrum of ZC can be attributed to ZIS vibration, which was also detected in annealed samples (Fig. S4b). The XRD and Raman patterns suggested that the crystal structure of both the as-obtained ZC

and its annealed samples remained unaltered. Fig. S5 gave the morphological characterization. The SEM image of the prepared ZC showed a composite nanofiber diameter of approximately 400 nm with uniformly distributed ZIS nanosheets on its surface (Fig. S5a). The EDX mappings in Fig. S6 confirmed the uniformly distribution of elements. TEM characterization of the as-obtained annealing product, ZC-1, unveiled a typical nanosheet structure of ZIS, which grew on the surface of CNFs (Fig. S5b and c). The CNFs demonstrated an amorphous state without visible lattice stripes, suggesting an absence of distinct diffraction peaks during X-ray diffraction testing. The HRTEM images of relevant areas revealed fringe spacing of 0.34 nm and 0.27 nm that pertain to the (102) and (006) planes of zinc iron spinel (ZIS), correspondingly. Notably, in regularly arranged lattice stripes, irregular segments emerged, which denoted the successful integration of oxygen doping (Fig. S5b). The ACTEM was commissioned to clarify the precise incorporation of oxygen doping into the composites. Oxygen atoms infiltrated the lattice structure of ZIS, taking the place of the original sulfur atoms after annealing in air. This caused a lattice distortion in ZIS due to the difference in the atoms of oxygen and sulfur (see Fig. S5d and e). The area surrounding the defect was marked by a dotted line, demonstrating the impact of O-doping in ZnIn_2S_4 on the occurrence of defects.

Doping can alter the chemical environment surrounding the replaced atom. Thus, we undertook XPS measurements to examine the chemical states of compounds (Fig. 2). In O 1 s spectra, the peak at 531.5 eV and 533.0 eV were attributed to -OH bond and absorbed O, respectively. As the temperature raised, ZIS becomes more reactive and easily combines with oxygen, resulting in the increase content of absorbed O. In addition, a peak of lattice O appeared at 529.9 eV and gradually increased with increasing temperature. This implied that unstable ZIS caused more S atoms to be substituted by O atoms at higher temperatures (Fig. 2a). It was worth noting that In 3d peak in Fig. 2b barely moved under treatment at 100°C , but the peak of In $3d_{5/2}$ started to shift negatively beyond 200°C . Furthermore, the intensity of this peak increased with the rise in annealing temperature. The motion was most evident at a temperature of 300°C , suggesting that O doping increased the electron density, resulting in the decrease of In's binding energy. The experimental results revealed that O would continuously penetrate the ZIS and displace the S atom as the temperature increased. Moreover, the ZIS arrangement remained stable after annealing at 300°C as no additional peak of In-O or Zn-O bonds appeared, indicating the absence of oxide. The electrochemical performance results demonstrate the performance changes brought about by o doping. The photocurrent response results showed that ZC-1 had the highest current density, indicating a rapid electron transfer (Fig. S7a). Fig. S7b represented that ZC-1 had the lowest overpotential for the photocatalytic reaction of ZC-1. Furthermore, electrochemical impedance spectroscopy revealed that ZC-1 provided the most favourable state for charge transfer (Fig. S7c). The resistance values of the analog circuit given in Table S1 also indicated that ZC-1 was most suitable for electron transfer in catalytic reactions.

3.3. Mechanism study of photogenerated electrons transfer

To investigate the role of oxygen doping in the photocatalytic process, we measured the hydrogen evolution activity and chemical performance of both O-doped ZC and pristine ZC samples. The sample after 100 degree annealing reached a maximum activity of $5736 \mu\text{mol} \cdot \text{g}^{-1} \cdot \text{h}^{-1}$, which is 9 and 2.5 times higher than that of ZIS and ZC (Fig. S8a). Clearly, the addition of oxygen had a significant impact on enhancing the performance of the photocatalyst. The cyclic test of ZC-1 shown in Figure S8b also proved that the material has good stability. Next, we conducted ISI-XPS analysis under different wavelength light irradiation (imported via an optical fiber) to determine the electronic structures and valence states under excited state conditions. Fig. 3 depicted the results of the analysis. The transfer of photogenerated electrons through the interface caused a modification in the outer electron density. Changes in binding energy exhibited an opposite trend to changes in outer electron

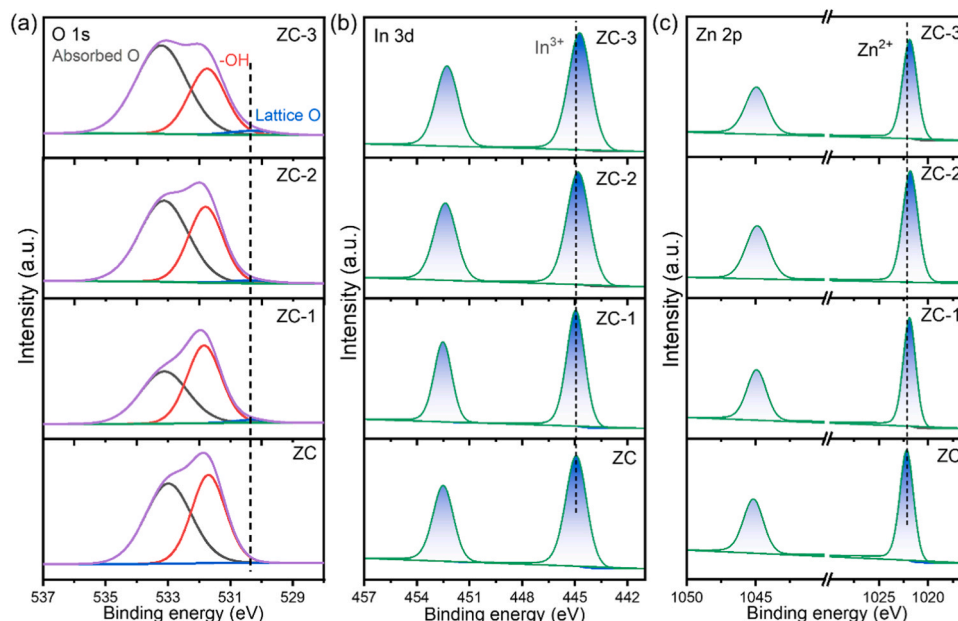


Fig. 2. The XPS narrow spectra of (a) O 1s, (b) In 3d and (c) Zn 2p of ZC-1.

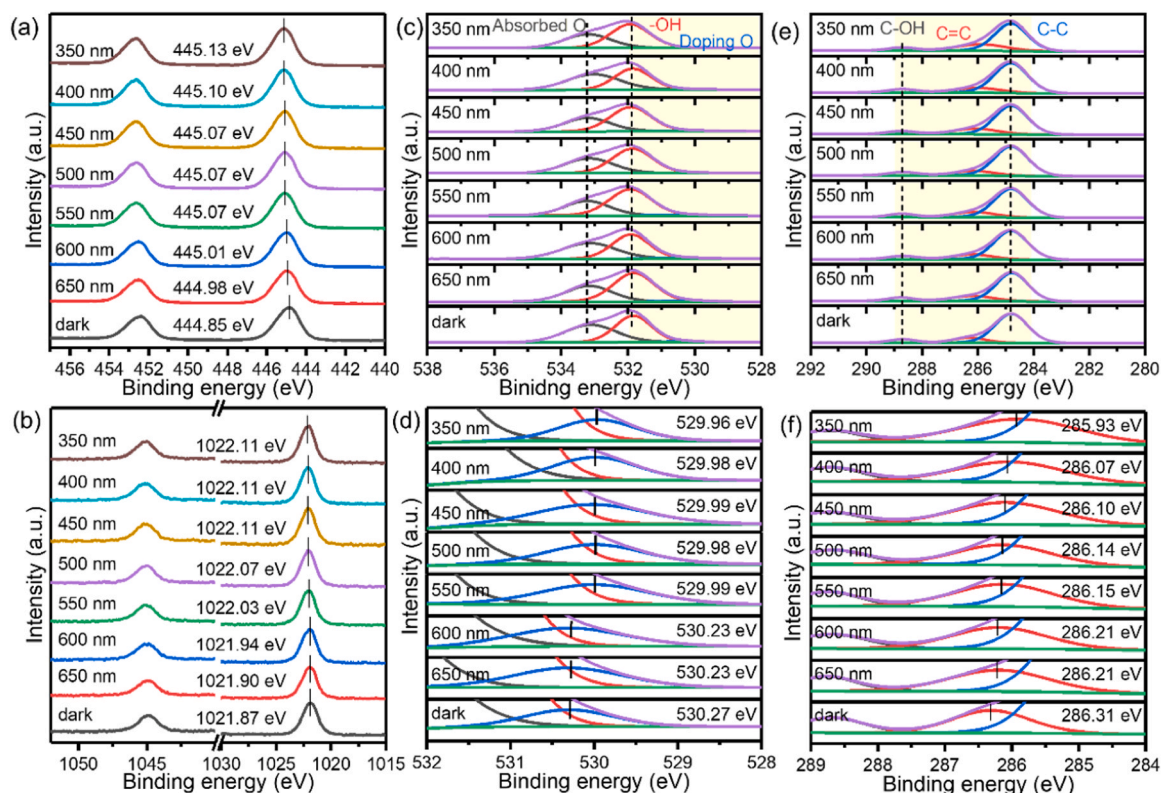


Fig. 3. The ISI-XPS results of (a) In 3d, (b) Zn 2p, (c, d) O 1s and (e, f) C 1s of ZC-1.

density. Based on the ISI-XPS results, both Zn 2p and In 3d shifted to a higher position, which suggested that photogenerated electrons flow from ZIS under incident light irradiation (Fig. 3a and b). Furthermore, we observed that the offset of binding energy increased when light was switched from red to violet, demonstrating that higher energy of incident light can enhance the migration of photogenerated electrons in a photocatalytic system. The study also examined the effect of oxygen doping. Fig. S9 displayed the ISI-XPS spectra of the pristine sample. The

binding energy shifts of In and Zn in ZC under 350 nm light irradiation were 0.14 eV and 0.13 eV, respectively (Fig. S9a and b). Interestingly, the shift of In and Zn in ZC-1 was 0.28 eV and 0.24 eV. This phenomenon was attributed to the introduction of oxygen doping, as demonstrated in Fig. 3a. Therefore, the investigation proceeded to examine the state of photogenerated electrons around O sites. Fig. 3c demonstrated that the -OH and absorbed O peaks were inactive when exposed to light, but the presence of doping O led to a red shift indicating the higher

concentration of electrons on the doping O site. The binding energy abruptly decreased from 530.27 eV to 529.99 eV at the wavelength of 550 nm and then remained basically stable, indicating that the doping O was a new photogenerated electron trapping site to promote the photocatalytic reaction (Fig. 4d). Furthermore, the shift in the C=C bond, which constituted the main component of CNFs, was noticeable in the annealing samples compared to ZC. Alterations in the C=C bond of the pristine sample were apparent in Fig. S9c and d. The initial binding energy of the C=C bond in ZC and ZC-1 was comparable, indicating that the doping of O did not impact the deeper structure of ZIS during 100 °C annealing. The outcome aligned well with the ex-situ XPS results. As the wavelength of the irradiated light decreased to 350 nm, there was a noticeable change in the shift of the C=C bond in both samples. It was worth highlighting that the C=C peak of the annealed sample displayed a more significant shift under the influence of the external light source. This observation suggested that more electrons had been transferred to CNFs. The results of the DFT simulation indicated that the introduction of O into ZIS had a direct impact on the electron structure, resulting in an increase in the number of photogenerated electrons under light irradiation. In this scenario, in addition to the buildup on the O site, increased photogenerated electrons may transfer from ZIS to CNFs, hastening the photocatalytic process. This occurrence demonstrated the rise in electron density in the composite due to O doping, which further facilitated the transfer of more photogenerated electrons to CNFs. The findings suggested that the introduced oxygen dopant can act as an electron trap, resulting in higher photocatalytic efficiency and increased electron density within the system. This was supported by the outcomes of DFT and ISI-XPS analysis.

In addition, XPS imaging provided a different approach to characterising changes in electron density by assessing the number of photo-excited electrons. An increase in outer-electron led to greater scattering during emission, which resulted in a reduction of emitted electrons and ultimately lowered the intensity of the image signal. Fig. S10 displayed the XPS imaging results of ZC-1 in the dark and in the illuminated situation. The imaging signal intensity had been normalized. However, the lack of clear observation of data points made it difficult to visually compare the signal variations before and after illumination. To ease comparison of the lighting impact, statistical data for imaging was provided in Fig. S11-13. From the statistical data, it could be observed that the signal strength variation within the 0.01 interval followed an approximate normal distribution. The supplementary information provided the details of the fitting process. Fig. 4 demonstrated the variation of each element under illumination. The total counts indicated the number of non-zero data points in the imaging. The amount of escape photoelectrons had a direct impact on signal intensity; therefore, reducing the number of outer electrons decreased the chances of scattering and allowed more electrons to escape. The opposite changes of Zn and In to O demonstrated the convergence of photogenerated electrons at the doping site, while the difference in area and FWHM reflected the concentration zone of signal intensity. The expansion of the observed

area revealed an increase in the number of emitted electrons, as more signals were being collected. The changes in the main parameters of various elements in light and dark environments suggested that photo-generated electrons migrate. The results from XPS imaging demonstrated that photogenerated electrons move from ZIS to doping O sites and participate in the recombination process of electrons and holes.

It was widely acknowledged that alterations in the chemical environment had a direct impact on the binding energy. Specifically, the gain and loss of electrons could affect the binding energy to varying degrees. To estimate the amount of electron migration, a comparison of binding energy changes pre- and post-illumination with light was made. Notably, there was a linear relationship between the binding energy and valence state (refer to Fig. S14-16). Based on the functional relationship obtained from the published research, the photogenerated electrons migrated differently for each element when the photocatalyst was exposed to irradiation light in a dark environment. The amount of photogenerated electrons transferred significantly increased with the introduction of O atoms into the lattice, resulting from changes in the valence state (Fig. S14). The valence changes of Zn increased from 0.48 to 0.89, while In increased from 0.29 to 0.59, as illustrated in Fig. S17a-d. Notably, In exhibited a higher degree of valence change than Zn, suggesting that S atom substitution by doping O occurred more frequently around In. Additionally, the valence changes of doping O before and after photoexcitation in the annealing sample were significant, as depicted in Fig. S18. The binding energy was measured at 530.27 eV, indicating a valence state of -2. This state was also common among O in many compounds. In the state of excitation, a reduction in the valence state from -2.10 to -2.99 indicated that some photogenerated electrons converged at the O site, thereby creating O as a new active site to boost photocatalytic activity. It was therefore evident that O doping had a significant impact on enhancing the photocatalytic activity. In addition, CNF demonstrated remarkable electrical conductivity, and its ultra-long fiber configuration could also provide numerous reaction sites. Fig. S17e and f demonstrated that the quantity of electron transfer rose by approximately 100 % following O doping. By performing ISI-XPS measurements and calculating electron transfer values, the study revealed the function of doped oxygen as active sites, leading to an increase in the level of charge transfer.

3.4. Calculation of charge utilization rate

It was accepted that the sluggish reaction kinetics could hinder the timely participation of photogenerated electrons in the photocatalytic reaction. Electrons that were isolated and did not participate in the reduction process lost their catalytic capacity through relaxation or quenching. Gaining a comprehension of the practical use of photogenerated electrons in catalytic reactions was crucial for designing effective photocatalysts. In light of the aforementioned circumstances, we proposed the utilization ratio (η) as a parameter to quantify the number of photogenerated electrons that could partake in the water

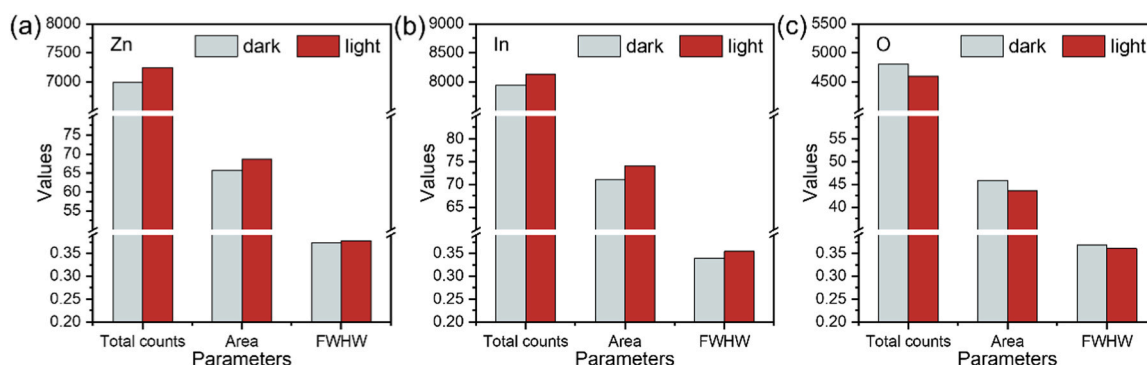


Fig. 4. The main parameters of XPS images of (a) In, (b) Zn and (c) O in ZC-1.

splitting reaction. Based on the above discussion, the photocatalytic performance under monochromatic light was tested to combine with valence state changes under the same monochromatic light in ISI-XPS. The apparent quantum yield (AQY) was a frequently employed method for characterizing the utilization of photons by catalysts. Fig. 5a and b presented the photocatalytic performance data along with the calculated AQY and η under monochromatic light. It was evident that the annealed sample exhibited superior photocatalytic performance and calculated AQY upon irradiation, indicating the beneficial impact of O doping. A more comprehensible illustration of the three parameters under monochromatic light was provided in Fig. 6c-e. The photocatalytic rate of H_2 evolution has noticeably increased, particularly in the visible range. Additionally, the AQY significantly improved, suggesting that the O dopant considerably enhances the photocatalyst's absorption of diverse light wavelengths. With regard to η , the utilization rate in the visible light range remained consistent before and after annealing. Interestingly, a variation in η was observed as the wavelength shifted from infrared to ultraviolet light. Upon exposure to 420 nm light, ZC-1 exhibited increased utilization of photogenerated electrons for photocatalytic reactions. Additionally, 18.0 % and 13.7 % of photogenerated electrons actively participated in H_2 reduction reactions under 365 nm incident light irradiation for ZC-1 and ZC, respectively. These findings demonstrated that the introduction of O could enrich the electron density of the system. As the total number of electrons generated by light excitation increased, a greater electron utilization was still achieved. This fully confirmed that doped O atoms could function as the active site during the photocatalytic reaction process.

3.5. Band structure investigation

After that, the band structure was applied to investigate the photo-generated electron transfer within the photocatalytic system [45–47]. Typically, the UV–vis DRS was employed to evaluate the light absorption ability of materials, and their corresponding band gap. Due to the remarkable conductivity of CNFs, they exhibited a full-spectrum absorption curve, which influenced the study of the optical properties of ZIS. Hence, bare ZIS was subjected to annealing at varying temperatures for the acquisition of UV–vis DRS measurement. For the pristine ZIS

sample, light with a wavelength longer than 500 nm was minimally utilized, as shown in Fig. S19. The light harvesting ability of ZIS-100 was significantly improved due to the electronic structure's modification, resulting in more electrons generated to absorb light after the introduction of O. The ZIS-200 exhibited a comparable trend to ZIS. Nonetheless, the ZIS-300 exhibited even weaker absorption of visible light compared to pristine ZIS, and slightly enhanced absorption of ultraviolet light. The band gap of all the prepared samples remained largely unchanged, indicating that the phase of ZIS was unaffected by O doping (Fig. 6a). The work function (Wf) was crucial in the study of electron transfer in duplicate semiconductor heterostructures. This parameter can be obtained by calculating the energy difference between the vacuum and Fermi levels based on the material's electrostatic potential [48–50]. Fig. 6b depicted that ZIS exhibited a Wf of 3.23 eV, whereas the annealed samples had Wf values of 2.34 eV, 2.56 eV and 3.93 eV, respectively. Based on the band gap and work function, the band positions of four prepared photocatalysts were determined (Fig. 6d). Notably, the conduction band (CB) position of ZIS-300 decreased to a lower position than that of the original sample. Additionally, the CB positions shifted to a more positive potential compared to the first two, indicating a weaker ability of photogenerated electrons to reduce on ZIS-300. The UPS analysis indicated that the CNFs displayed a cut-off edge of 16.92 eV and a Fermi edge of 0.02 eV, implying strong conductivity (Fig. S20). The UPS results further suggested that electrons flowed from ZIS to CNFs due to the lower Wf of CNFs in comparison to ZIS. Due to the lower Fermi level position of CNFs, electrons from ZIS would flow through the interface towards CNFs. With the loss of electrons, the Fermi level of ZIS would gradually drop until it was consistent with CNFs (Fig. 6e). This led to the formation of a depletion layer around CNFs in the energy band of ZIS, causing electron accumulation on the surface of CNFs. When the two Fermi levels were equalized, a Schottky barrier formed at the heterojunction. When the ZIS was exposed to light, the electrons generated by the photocatalytic reaction moved from the valence band (VB) to CB and ultimately migrated to CNFs to participate in the reaction. The Schottky barrier inhibited the backflow of electrons to the ZIS. The annealed samples demonstrated the same behaviour as those in contact with CNFs. Oxygen doping led to the formation of a new defect band (DB) close to the CB of ZIS, as confirmed

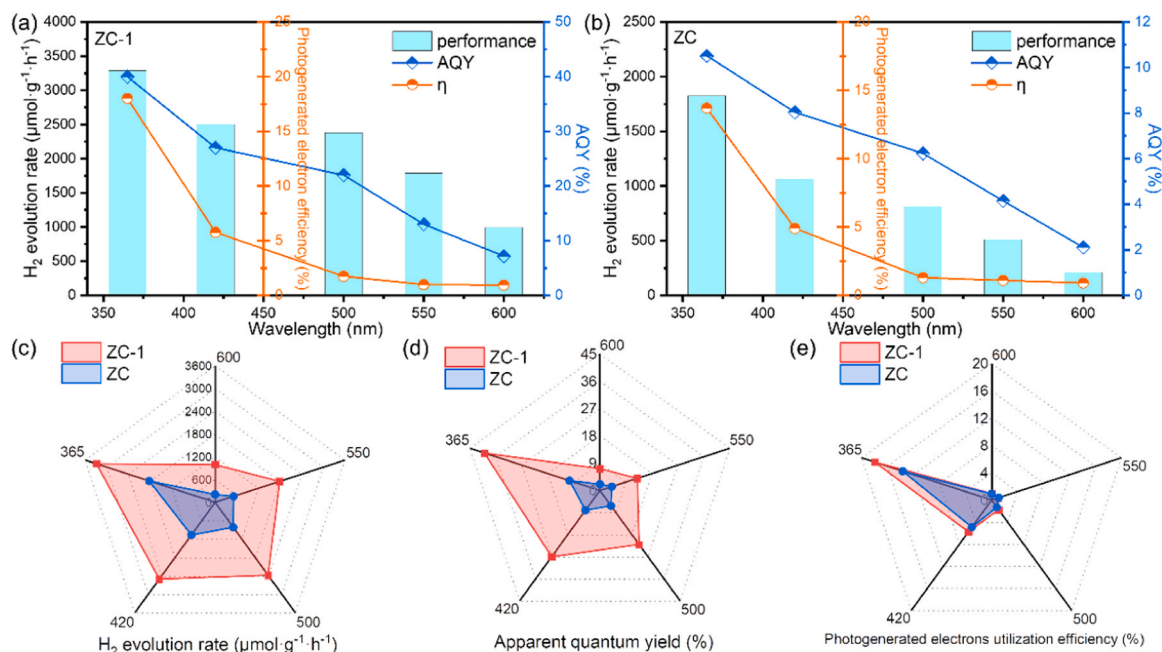


Fig. 5. The photogenerated electrons utilization ratio of (a) ZC-1 and (b) ZC. Comparison of the performance parameters of ZC-1 and ZC in (c) H_2 evolution rate, (d) AQY and (e) η .

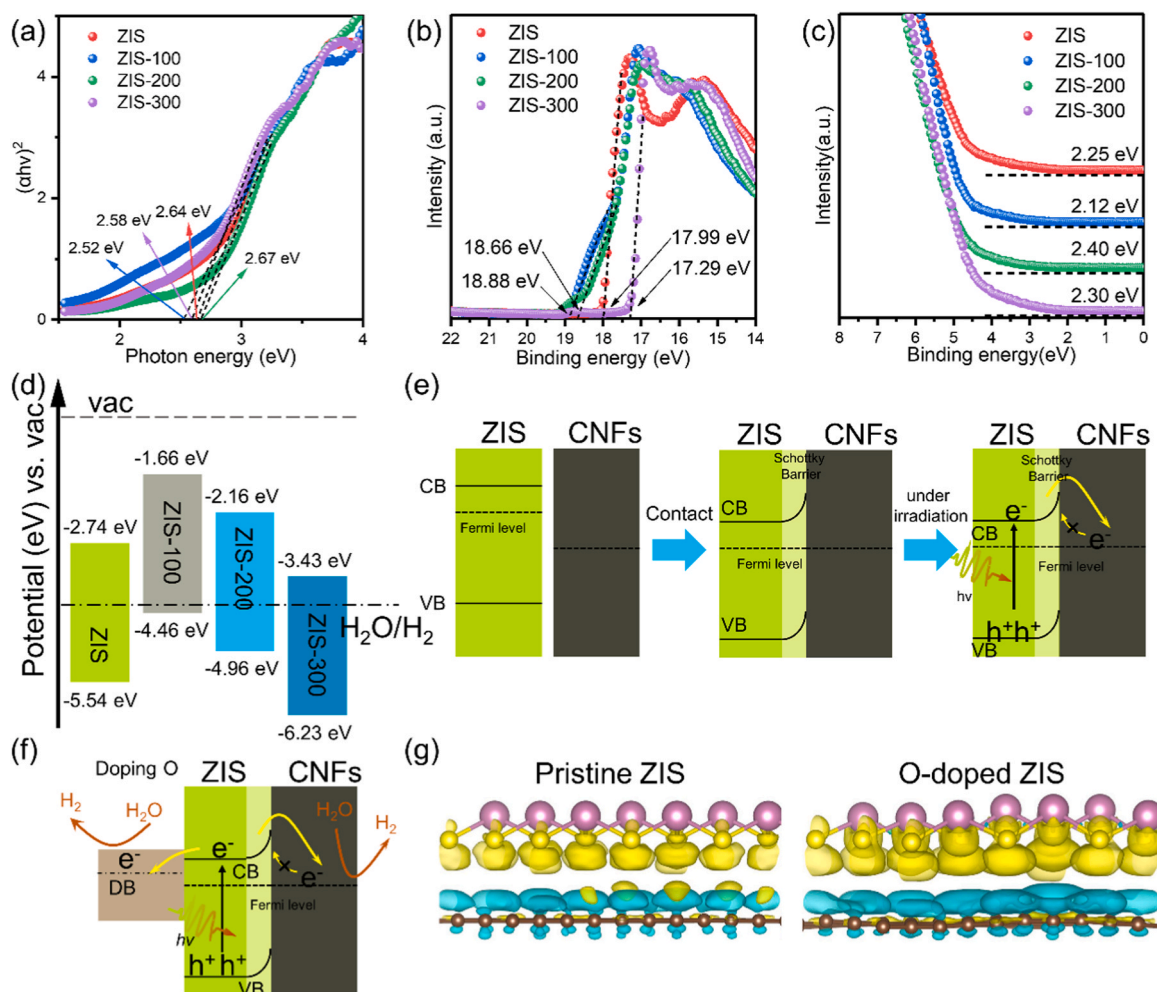


Fig. 6. (a) The calculated band gap, (b) The cut-off edge and (c) fermi edge and (d) Band structure alignments for of pristine and annealing ZIS. (e) Schottky barrier formation based on Fermi level difference. (f) The photogenerated electrons transfer pathway in ZC-1. (g) The differential charge density before and after doping.

by the UV-vis DRS curve. As displayed in Fig. S21, an additional absorption peak emerged due to lattice defects and disorders. The energy difference between the valence band and defect band could be calculated as 1.75 eV. The creation of new defect bands near the conduction band efficiently hindered the recombination of photogenerated electrons. According to the outcomes of ISI-XPS, the oxygen dopant acted as an electron collector. The generated electrons could transfer to both the carbon nanofibres and oxygen sites to facilitate the reduction of H_2O to H_2 . The bi-directional transmission of photogenerated electrons significantly lowered the intrinsic recombination efficiency and enhanced the activity of the composite (Fig. 6f). Fig. 6g displayed the differential charge density of pristine and O-doped ZIS, where cyan and yellow denote electron accumulation and depletion layers respectively. The calculation results revealed that upon replacement of the S atom with the O atom, the heterojunction's depletion and accumulation layer scale grew notably larger, signifying a significant surge in electron transfer.

4. Conclusion

In summary, we developed an O-doped ZIS hybrid catalyst using a straightforward heat treatment method in air. This catalyst allowed us to analyze the behavior of photogenerated electrons at the heterointerface in a systematic manner. Our investigation of the photogenerated electron amount calculation process had established an experimental paradigm for the disclose of intricate mechanisms in photocatalysis. This approach permitted us to utilize ISI-XPS techniques more efficiently.

These findings demonstrated that O-doped sites can function as a reaction center, accelerating the process of photocatalytic water splitting. Additionally, we introduced a parameter to describe the efficacy of utilizing photogenerated electrons in evaluating the performance of the photocatalyst. Our study provided an alternative approach for studying the mechanics of photocatalysts and sheds light on the potential applications of ISI-XPS.

CRediT authorship contribution statement

Guosheng Shao: Resources, Funding acquisition, Conceptualization. **Peng Zhang:** Writing – review & editing, Validation, Supervision, Methodology, Funding acquisition, Conceptualization. **Zuhao Shi:** Visualization, Software, Methodology. **Meng Cai:** Writing – review & editing, Validation, Investigation. **Yinyin Ai:** Writing – review & editing, Validation. **Ruohan Hou:** Writing – review & editing, Validation, Investigation. **Yongshang Zhang:** Resources, Investigation, Conceptualization. **Yukun Li:** Writing – original draft, Validation, Investigation, Data curation, Conceptualization.

Declaration of Competing Interest

The authors declare that they have no known competing financial interests or personal relationships that could have appeared to influence the work reported in this paper.

Data availability

Data will be made available on request.

Acknowledgement

The work was supported by the National Natural Science Foundation of China (No. 51972287, U2004172, 51502269), the National Natural Science Foundation of Henan Province (No. 242300421008, 222301420039), the Foundation for University Key Teacher of Henan Province (2020GGJS009) and Sponsored by Program for Science & Technology Innovation Talents in Universities of Henan Province (23HASTIT001).

Appendix A. Supporting information

Supplementary data associated with this article can be found in the online version at [doi:10.1016/j.apcatb.2024.124223](https://doi.org/10.1016/j.apcatb.2024.124223).

References

- Q. Zhu, Q. Xu, M. Du, X. Zeng, G. Zhong, B. Qiu, J. Zhang, Recent progress of metal sulfide photocatalysts for solar energy conversion, *Adv. Mater.* 34 (2022) 2202929.
- H. Wang, Y. Tian, B. König, Energy- and atom-efficient chemical synthesis with endergonic photocatalysis, *Nat. Rev. Chem.* 6 (2022) 745–755.
- T.P. Yoon, M.A. Ischay, J. Du, Visible light photocatalysis as a greener approach to photochemical synthesis, *Nat. Chem.* 2 (2010) 527–532.
- G. Cao, N.A. Deskins, N. Yi, Carbon monoxide oxidation over copper and nitrogen modified titanium dioxide*, *Appl. Catal., B: Environ.* 285 (2021) 119748.
- C. Bie, L. Wang, J. Yu, Challenges for photocatalytic overall water splitting, *Chem* 8 (2022) 1567–1574.
- A. Fujishima, K. Honda, Electrochemical photolysis of water at a semiconductor electrode, *Nature* 238 (1972) 37–38.
- S. Cheng, Z. Sun, K.H. Lim, T.Z.H. Gani, T. Zhang, Y. Wang, H. Yin, K. Liu, H. Guo, T. Du, L. Liu, G.K. Li, Z. Yin, S. Kawi, Emerging strategies for CO₂ photoreduction to CH₄: from experimental to data-driven design, *Adv. Energy Mater.* 12 (2022) 2200389.
- C. Feng, Z. Wu, K. Huang, J. Ye, H. Zhang, Surface modification of 2D photocatalysts for solar energy conversion, *Adv. Mater.* 34 (2022) 2200180.
- K. Huang, J. Bai, R. Shen, X. Li, C. Qin, P. Zhang, X. Li, Boosting photocatalytic hydrogen evolution through local charge polarization in chemically bonded single-molecule junctions between ketone molecules and covalent organic frameworks, *Adv. Funct. Mater.* 33 (2023) 2307300.
- Z. Zhang, X. Huang, Y. Bi, High-efficiency and stable syngas production by coupling NiFe-BiVO₄ photoanodes with AgOx/Ag cathodes, *Appl. Catal. B: Environ. Energy* 349 (2024) 123894.
- G. Ren, J. Zhao, Z. Zhao, Z. Li, L. Wang, Z. Zhang, C. Li, X. Meng, Defects-induced single-atom anchoring on metal-organic frameworks for high-efficiency photocatalytic nitrogen reduction, *Angew. Chem. Int. Ed.* 63 (2024) e202314408.
- Y. Li, L. Wang, F. Zhang, W. Zhang, G. Shao, P. Zhang, Detecting and quantifying wavelength-dependent electrons transfer in heterostructure catalyst via in situ irradiation XPS, *Adv. Sci.* 10 (2023) 2205020.
- L. Wang, Y. Li, C. Wu, X. Li, G. Shao, P. Zhang, Tracking charge transfer pathways in SrTiO₃/CoP/Mo₂C nanofibers for enhanced photocatalytic solar fuel production, *Chin. J. Catal.* 43 (2022) 507–518.
- X. Ruan, C. Huang, H. Cheng, Z. Zhang, Y. Cui, Z. Li, T. Xie, K. Ba, H. Zhang, L. Zhang, X. Zhao, J. Leng, S. Jin, W. Zhang, W. Zheng, S.K. Ravi, Z. Jiang, X. Cui, J. Yu, A twin S-scheme artificial photosynthetic system with self-assembled heterojunctions yields superior photocatalytic hydrogen evolution rate, *Adv. Mater.* 35 (2023) 2209141.
- H. Gu, H. Zhang, X. Wang, Q. Li, S. Chang, Y. Huang, L. Gao, Y. Cui, R. Liu, W. Dai, Robust construction of CdSe nanorods/Ti₃C₂ MXene nanosheet for superior photocatalytic H₂ evolution, *Appl. Catal., B: Environ.* 328 (2023) 122537.
- X. Xu, L. Meng, J. Zhang, S. Yang, C. Sun, H. Li, J. Li, Y. Zhu, Full-spectrum responsive naphthalimide/perylene diimide with a giant internal electric field for photocatalytic overall water splitting, *Angew. Chem. Int. Ed.* 63 (2024) e202308597.
- P. Zhang, Y. Li, Y. Zhang, R. Hou, X. Zhang, C. Xue, S. Wang, B. Zhu, N. Li, G. Shao, Photogenerated electron transfer process in heterojunctions: in situ irradiation XPS, *Small Methods* 4 (2020) 2000214.
- L. Cheng, X. Yue, L. Wang, D. Zhang, P. Zhang, J. Fan, Q. Xiang, Dual-single-atom tailoring with bifunctional integration for high-performance CO₂ photoreduction, *Adv. Mater.* 33 (2021) 2105135.
- L. Cheng, P. Zhang, Q. Wen, J. Fan, Q. Xiang, Copper and platinum dual-single-atoms supported on crystalline graphitic carbon nitride for enhanced photocatalytic CO₂ reduction, *Chin. J. Catal.* 43 (2022) 451–460.
- P. Xie, J. Ding, Z. Yao, T. Pu, P. Zhang, Z. Huang, C. Wang, J. Zhang, N. Zecher-Freeman, H. Zong, D. Yuan, S. Deng, R. Shahbazian-Yassar, C. Wang, Oxo dicopper anchored on carbon nitride for selective oxidation of methane, *Nat. Commun.* 13 (2022) 1375.
- W. Zhang, Y. Li, L. Wang, F. Zhang, Y. Ai, G. Shao, P. Zhang, In situ construction of cyano-modified g-C₃N₄ nanolayer-coated SrTiO₃ nanotubes by gas-solid reaction for efficient photocatalytic solar fuel production, *Chem. Eng. J.* 469 (2023) 143817.
- Y. Liu, Y. Sun, E. Zhao, W. Yang, J. Lin, Q. Zhong, H. Qi, A. Deng, S. Yang, H. Zhang, H. He, S. Liu, Z. Chen, S. Wang, Atomically dispersed silver-cobalt dual-metal sites synergistically promoting photocatalytic hydrogen evolution, *Adv. Funct. Mater.* 33 (2023) 2301840.
- Y. Shen, C. Ren, L. Zheng, X. Xu, R. Long, W. Zhang, Y. Yang, Y. Zhang, Y. Yao, H. Chi, J. Wang, Q. Shen, Y. Xiong, Z. Zou, Y. Zhou, Room-temperature photosynthesis of propane from CO₂ with Cu single atoms on vacancy-rich TiO₂, *Nat. Commun.* 14 (2023) 1117.
- W. Xie, K. Li, X. Liu, X. Zhang, H. Huang, P-Mediated Cu–N₄ sites in carbon nitride realizing CO₂ photoreduction to C₂H₄ with selectivity modulation, *Adv. Mater.* 35 (2023) 2208132.
- W. Zou, Y. Cheng, Y. Ye, X. Wei, Q. Tong, L. Dong, G. Ouyang, Metal-free photocatalytic CO₂ reduction to CH₄ and H₂O₂ under non-sacrificial ambient conditions, *Angew. Chem. Int. Ed.* 62 (2023) e202313392.
- M.J. Zachman, V. Fung, F. Polo-Garzon, S. Cao, J. Moon, Z. Huang, D. Jiang, Z. Wu, M. Chi, Measuring and directing charge transfer in heterogeneous catalysts, *Nat. Commun.* 13 (2022) 3253.
- X. Li, C. Wang, J. Tang, Methane transformation by photocatalysis, *Nat. Rev. Mater.* 7 (2022) 617–632.
- P. Liu, Z. Huang, X. Gao, X. Hong, J. Zhu, G. Wang, Y. Wu, J. Zeng, X. Zheng, Synergy between palladium single atoms and nanoparticles via hydrogen spillover for enhancing CO₂ photoreduction to CH₄, *Adv. Mater.* 34 (2022) 2200057.
- R. Zeng, C. Cheng, F. Xing, Y. Zou, K. Ding, C. Huang, Dual vacancies induced local polarization electric field for high-performance photocatalytic H₂ production, *Appl. Catal., B: Environ.* 316 (2022) 121680.
- K. Zhu, Q. Zhu, M. Jiang, Y. Zhang, Z. Shao, Z. Geng, X. Wang, H. Zeng, X. Wu, W. Zhang, K. Huang, S. Feng, Modulating Ti t_{2g} orbital occupancy in a Cu/TiO₂ composite for selective photocatalytic CO₂ reduction to CO, *Angew. Chem. Int. Ed.* 61 (2022) e202207600.
- Y. Sun, C. Xue, L. Chen, Y. Li, S. Guo, Y. Shen, F. Dong, G. Shao, P. Zhang, Enhancement of interfacial charge transportation through construction of 2D–2D p–n Heterojunctions in hierarchical 3D CNFs/MoS₂/ZnIn₂S₄ composites to enable high-efficiency photocatalytic hydrogen evolution, *Sol. RRL* 5 (2021) 2000722.
- J. Wan, L. Liu, Y. Wu, J. Song, J. Liu, R. Song, J. Low, X. Chen, J. Wang, F. Fu, Y. Xiong, Exploring the polarization photocatalysis of ZnIn₂S₄ material toward hydrogen evolution by integrating cascade electric fields with hole transfer vehicle, *Adv. Funct. Mater.* 32 (2022) 2203252.
- L. Zhao, B. Yang, G. Zhuang, Y. Wen, T. Zhang, M. Lin, Z. Zhuang, Y. Yu, Thin in-plane In₂O₃/ZnIn₂S₄ heterostructure formed by topological-atom-extraction: optimal distance and charge transfer for effective CO₂ photoreduction, *Small* 18 (2022) 2201668.
- J. Li, C. Tan, M. Qi, Z. Tang, Y. Xu, Exposed zinc sites on hybrid ZnIn₂S₄/CdS nanocages for efficient regioselective photocatalytic epoxide alcoholysis, *Angew. Chem. Int. Ed.* 62 (2023) e202303054.
- C. Tan, M. Qi, Z. Tang, Y. Xu, Cocatalyst decorated ZnIn₂S₄ composites for cooperative alcohol conversion and H₂ evolution, *Appl. Catal. B: Environ.* 298 (2021) 120541.
- X. Wang, T. Shi, X. Wang, G. Li, L. Wang, J. Huang, A. Meng, Z. Li, Low-valent cation doping and leaching to construct single-atom Cu decorated Cu–ZnIn₂S₄ with multiple defects for boosting photocatalytic H₂ evolution, *Appl. Catal. B: Environ. Energy* 348 (2024) 123807.
- W. Zhan, X. Zhang, Y. Yuan, Q. Weng, S. Song, M.d.J. Martínez-López, J.L. Arauz-Lara, F. Jia, Regulating chemisorption and electroosorption activity for efficient uptake of rare earth elements in low concentration on oxygen-doped molybdenum disulfide, *ACS Nano* 18 (2024) 7298–7310.
- R.K. Chava, N. Son, M. Kang, Controllable oxygen doping and sulfur vacancies in one dimensional CdS nanorods for boosted hydrogen evolution reaction, *J. Alloy. Compd.* 873 (2021) 159797.
- X. Long, C. Feng, S. Yang, D. Ding, J. Feng, M. Liu, Y. Chen, J. Tan, X. Peng, J. Shi, R. Chen, Oxygen doped graphitic carbon nitride with regulatable local electron density and band structure for improved photocatalytic degradation of bisphenol A, *Chem. Eng. J.* 435 (2022) 134835.
- Y. Zhang, Z. Hu, H. Zhang, H. Li, S. Yang, Uncovering Original Z Scheme Heterojunctions of COF/MOx (M = Ti, Zn, Zr, Sn, Ce, and Nb) with Ascendant Photocatalytic Selectivity for Virtually 99.9% NO-to-NO₃– Oxidation, *Adv. Funct. Mater.* 33 (2023) 2303851.
- J. Zhou, B. Gao, D. Wu, C. Tian, H. Ran, W. Chen, Q. Huang, W. Zhang, F. Qi, N. Zhang, Y. Pu, J. Qiu, Z. Hu, J. Du, Z. Liu, Y. Leng, X. Tang, Enhanced photocatalytic activity of lead-free Cs₂TeBr₆/g-C₃N₄ heterojunction photocatalyst and its mechanism, *Adv. Funct. Mater.* 34 (2024) 2308411.
- F. Li, L. Cheng, J. Fan, Q. Xiang, Steering the behavior of photogenerated carriers in semiconductor photocatalysts: a new insight and perspective, *J. Mater. Chem. A* 9 (2021) 23765–23782.
- Z. Liu, Z. Zhao, W. Jiang, Z. Zhu, Y. Wang, Z. Liu, W. Gu, Y. Yang, Y. Yang, L. Zhang, W. Yao, F. Teng, Structural reconstruction of carbon nitride with tailored electronic structure: a bifunctional photocatalyst for cooperative artificial photosynthesis and selective phenylcarbinol oxidation, *Appl. Catal., B: Environ.* 298 (2021) 120517.
- M. Wang, S. Xu, Z. Zhou, C. Dong, X. Guo, J. Chen, Y. Huang, S. Shen, Y. Chen, L. Guo, C. Burda, Atomically dispersed janus nickel sites on red phosphorus for photocatalytic overall water splitting, *Angew. Chem. Int. Ed.* 61 (2022) e202204711.

- [45] R. Hou, S. Zhang, P. Zhang, Y. Zhang, X. Zhang, N. Li, Z. Shi, G. Shao, Ti_3C_2 MXene as an “energy band bridge” to regulate the heterointerface mass transfer and electron reversible exchange process for Li–S batteries, *J. Mater. Chem. A* 8 (2020) 25255–25267.
- [46] P. Zhang, Y. Zhao, Y. Li, N. Li, S.R.P. Silva, G. Shao, P. Zhang, Revealing the selective bifunctional electrocatalytic sites via in situ irradiated x-ray photoelectron spectroscopy for lithium–sulfur battery, *Adv. Sci.* 10 (2023) 2206786.
- [47] R. Hou, Y. Li, Z. Wang, Z. Shi, N. Li, F. Miao, G. Shao, P. Zhang, In situ 1D carbon chain-mail catalyst assembly for stable lithium–sulfur full batteries, *Small* 19 (2023) 2300868.
- [48] R. Hou, S. Zhang, Y. Zhang, N. Li, S. Wang, B. Ding, G. Shao, P. Zhang, A “Three-Region” configuration for enhanced electrochemical kinetics and high-area capacity lithium–sulfur batteries, *Adv. Funct. Mater.* 32 (2022) 2200302.
- [49] P. Zhang, S. Zhang, D. Wan, P. Zhang, Z. Zhang, G. Shao, Multilevel polarization-fields enhanced capture and photocatalytic conversion of particulate matter over flexible schottky-junction nanofiber membranes, *J. Hazard. Mater.* 395 (2020) 122639.
- [50] Y. Zhang, P. Zhang, S. Zhang, Z. Wang, N. Li, S.R.P. Silva, G. Shao, A flexible metallic TiC nanofiber/vertical graphene 1D/2D heterostructured as active electrocatalyst for advanced Li–S batteries, *InfoMat* 3 (2021) 790–803.